Nuclear Inst. and Methods in Physics Research, A 870 (2017) 131–139

Contents lists available at ScienceDirect

Nuclear Inst. and Methods in Physics Research, A

journal homepage: www.elsevier.com/locate/nima

# Design optimization for a wearable, gamma-ray and neutron sensitive, detector array with directionality estimation

Birsen Ayaz-Maierhafer [a,*], Carl G. Britt [a], Andrew J. August [a], Hairong Qi [a], Carolyn E. Seifert [b], Jason P. Hayward [a,c]

[a] University of Tennessee, Department of Nuclear Engineering, Pasqua Nuclear Engineering Building, 1004 Estabrook Road, Knoxville, TN 37996, United States
[b] Pacific Northwest National Laboratory (PNNL), 902 Battelle Blvd, Richland, WA 99354, United States
[c] Oak Ridge National Laboratory, 1 Bethel Valley Rd, Oak Ridge, TN 37830, United States

ARTICLE INFO

*Keywords:*
Backpack detectors
Nonproliferation
Gamma-ray and neutron detectors
kNN
MCNP
Directionality estimation

ABSTRACT

In this study, we report on a constrained optimization and tradeoff study of a hybrid, wearable detector array having directional sensing based upon gamma-ray occlusion. One resulting design uses CLYC detectors while the second feasibility design involves the coupling of gamma-ray-sensitive CsI scintillators and a rubber $LiCaAlF_6$ (LiCAF) neutron detector. The detector systems' responses were investigated through simulation as a function of angle in a two-dimensional plane. The expected total counts, peak-to-total ratio, directionality performance, and detection of $^{40}K$ for accurate gain stabilization were considered in the optimization. Source directionality estimation was investigated using Bayesian algorithms. Gamma-ray energies of 122 keV, 662 keV, and 1332 keV were considered. The equivalent neutron capture response compared with $^{3}He$ was also investigated for both designs.



## 1. Introduction

The detection and localization of radiological and nuclear materials via search is a challenging problem. To address this challenge, the U.S. federal government has supported many research programs are continuing to investigate vehicle- and person-carried systems including larger coded aperture imagers [1,2], handheld devices [3], and backpack-mounted sensors [4–7].

Many backpack-based systems have been studied and manufactured, some having directional sensitivity. For example, The Bruker Detection Corporation developed a system called the Radiation Backpack Sentry [4]. Their technology utilizes a 7.62 cm × 7.62 cm NaI:Tl crystal that provides sensitivity for gamma-ray isotopic identification. Symmetrica's VeriFinder™ Backpack uses a NaI:Tl crystal for gamma-ray detection and ZnS:Ag/$^{6}$LiF blade modules for neutron detection [5]. Another recent commercial device, the Rapiscan MP100 backpack, uses polyvinyl toluene (PVT) plastic scintillator gamma-ray detectors for directional sensitivity and $^{10}$B-based neutron detectors; the gamma-ray and neutron detection performance also meet the requirements of ANSI N42.53 [6]. The Thermo Scientific™ PackEye Radiation Detection Backpack can locate gamma-ray-emitting radioactive sources via plastic scintillators; it uses two flat Li-6 doped scintillators for neutron detection [7]. This detector system also has localization capabilities.

In addition, there is some ongoing research and development of backpack-based detector designs. For example, Lacy et al., published research on using boron-coated-straw (BCS) detectors in a backpack [8]. Their module consisted of 36 BCS tubes, arranged in two rows, together with a plastic scintillator for gamma-ray detection and acting as a moderator for high-energy neutrons. Recently, McDonald, et al., developed a wearable system based on two CLYC scintillators, allowing for simultaneous gamma-ray and neutron detection [9]. Furthermore, Nilsson, et al., investigated the performance of three backpack-mounted, gamma-radiation survey systems using detectors made of $LaBr_3$:Ce, NaI(Tl), or HPGe [10]. This detection system has mapping capabilities.

The aforementioned detector systems have their own unique capabilities, but research in the literature on wearable systems capable of gamma-based directionality estimation using a simple set of close-packed detector arrays is particularly lacking, leading to an inadequate understanding in the community about how to best design and build a deployable system. Here, we are investigating a directionally-capable backpack that has the potential to detect, locate, and identify radiological and nuclear sources quickly. To be clear, a directionally-capable

* Corresponding author.
*E-mail address:* bayazmai@utk.edu (B. Ayaz-Maierhafer).

http://dx.doi.org/10.1016/j.nima.2017.07.020
Received 25 April 2017; Received in revised form 3 June 2017; Accepted 12 July 2017
Available online 27 July 2017
0168-9002/

system can estimate the direction to a radioactive source even while the system and the source are stationary. Detection and identification tasks require sensing systems that maximize the source counts and peak-to-total ratio from a nuclear or radiological threat, while maintaining gain stabilization, either through an internal source or tracking the $^{40}$K peak present in NORM [11].

In this work, we report on the constrained optimization of a hybrid, backpack-based, detector array having directional sensitivity based upon gamma occlusion. A separate paper describes methods to estimate the instantaneous direction of a gamma source based upon such a close-packed gamma detector array [12]. This paper reports on a constrained optimization leading to two different buildable designs. Furthermore, we show how design selections for wearable designs involve expected tradeoffs between system performance parameters including gamma and neutron detection efficiency, directional performance, gamma photopeak efficiency, and intrinsic gain stability.

## 2. Monte Carlo simulation studies

In this section, we present the Monte Carlo simulations used to generate our data and our associated directionality study and gain stabilization study. MCNP6 was used because it has been well validated for gamma-ray and neutron transport [13,14]. Next, design selections are made based upon these results.

We describe two different designs. The first design uses $Cs_2LiYCl_6$:Ce (CLYC) detectors alone. Since CLYC detectors have sensitivity to both gamma-ray and neutron radiation [15,16], an additional neutron detector was not necessary in the design. The second design is a hybrid of a gamma-ray-sensitive CsI:Na scintillator array and a Transparent Rubber SheeT (TRUST) type $LiCaAlF_6$:Ce (LiCAF) [17,18] neutron scintillator. The detector systems' responses were investigated as a function of angle. In our simulation study, the mass of the neutron- and gamma-ray-sensitive scintillator was fixed at either 3 or 4 kg in order to consider lightweight systems. Our recent experience for a three detector system shows that the total detector mass is 50% greater than the scintillator mass, including detector housing and compact, silicon photomultiplier-based electronics; thus, for example, a 4 kg system could be expected to have mass of 6 kg in practice. Looking at results for these two different masses allows one to understand what may be expected when either more detector mass is added for additional sensitivity or some gamma-ray detector mass is taken away to add more sensitivity to neutrons (when the gamma detectors are not also sensitive to neutrons).

### 2.1. Monte Carlo simulations for gamma-ray sensing

Several sets of MCNP6.1 simulations were performed: one set to produce data to investigate the gamma-ray response (for CLYC and CsI:Na) and one set to investigate neutron response (for CLYC, LiCAF or $^3$He detectors) for our hybrid systems.

The MCNP simulations consisted of a human body phantom—with specifications given in American National Standard performance criteria for Backpack Based Radiation-Detection Systems (ANSI used for homeland security, 42.53-2013) [19]; between 2–6 radiation detectors; and a radioactive source located at 1 m. The exterior of the first detector crystal(s) (close to the phantom, first row) was placed 3 cm away from the phantom, and neighboring detector crystals were placed 5 mm apart initially. An example detector geometry comprised of 3 Right Parallelepiped (RPP) detectors is shown in Fig. 1(a). To simulate the possible directions to the source, thirty-seven simulations were performed—one for each source-angle from 0° to 180° in increments of 5° (See Fig. 1(b)). Simulations were not performed from 185° to 355° due to the radial symmetry of the investigated geometry. Note that the angle is measured clockwise from the normal to the center of the phantom's back. The distance $r$ from the source to the center of the backpack detector array was 1 m in all simulations; the expected counts at greater distances may be easily estimated based upon a $1/r^2$ reduction. To tally the expected events from each detector, we used an F8 pulse-height tally (a tally of energy deposition for detector interactions) with a threshold energy of 60 keV, assuming that some threshold around this value may be used to discriminate against gamma-ray background and electronic noise. Gamma-ray and neutron backgrounds were not simulated for this study, so our analysis represents the limit of what may be achieved under ideal conditions. Gamma-ray sources were modeled as monoenergetic zero-mass point sources with energies of 122, 662, and 1332 keV. The 122 and 1332 keV sources were used only in some selected configurations to understand the response from low and high energy gammas.

Our study considered both compact (5 mm crystal separation) and loose detector array configurations comprised of 2, 3, 4, 5 or 6 detectors. The loose detector configurations have at least two detectors and these detectors are separated at least one detector size as shown in Fig. 2(b), (e), (g), (i). We limited the maximum number of detectors to six in order to limit system complexity and cost. We desired detector shapes that had lower surface-area-to-volume ratios, which were also easy to fabricate and optically read out, so we considered either Right Circular Cylinder (RCC) or Right Perpendicular Parallelepiped (RPP) shapes. Lower surface-area-to-volume ratios should be beneficial for higher photopeak efficiency, especially at higher gamma energies including 1461 keV, which impacts the intrinsic ability to keep a detector system gain stabilized using the naturally occurring 1461 keV photopeak from $^{40}$K. This is clearly true in the extreme case of a very thin sheet (high surface area) vs. a sphere (low surface area), each having the same volume.

Nine different detector configurations were considered, one for 2 detectors, two for 3 detectors, two for 4 detectors, two for 5 and two for 6 detectors in the array. The 3, 4, 5 and 6 detector configurations were in compact (C) or loose (L) forms. Each configuration was simulated with RCC and RPP detector shapes. The nine detector configurations with RPP-shaped detectors are illustrated in Fig. 2. A total of 37 simulations (from 0° to 180° in 5° increments) were performed for each detector configuration, and this set of simulations was done for two detector materials (CLYC or CsI:Na), two detector shapes (RPP and RCC), two total masses of detector (3 or 4 kg), and for varying detector dimensions, given these fixed masses. When more detectors are present in the array, the length of each detector is reduced accordingly to maintain total detector mass. Dimensions (diameter or length) of 5.08 cm (2 in.), 7.62 cm (3 in.) or 5.38 cm were used for the comparably less dense CLYC detectors ($\rho_{CLYC} = 3.31$ g/cm$^3$), while dimensions of 4 cm, 4.5 cm or 5.08 cm (2 in.) were used for the comparably more dense CsI:Na detectors ($\rho_{CsI} = 4.5$ g/cm$^3$). More information on the simulations is given in Table 1. The "/" in Table 1 represents a division in the data for either a RPP or a RCC shape.

Fig. 3 shows the 1-s angular detector response to a 1 $\mu$Ci $^{137}$Cs source for 2-C, 3-C, 3-L, 4-C, 5-L and 6-L configurations of a 4-kg CLYC detector array. As expected, for each configuration the response for each detector is highly dependent on the angle to the source. The complexity of the response increases with an increase in the number of detectors. If one pays attention to the 3-L (Fig. 3(b)) and 3-C (Fig. 3(c)) configurations, one can see how the count rates differ for similar detector geometries because of the change in occlusion of one detector by another. Also, notice that with an increasing number of the detectors the total counts per detector tend to decrease because each detector's height and therefore vertical surface area per detector decreases as well.

The total counts for any configuration may be obtained by summing the responses from each detector, as shown in Fig. 4(a). This analysis ignores timing coincidence. Notice that the count rates tend to be lower when the detectors are occluded by the phantom, especially at high angles (~110°–140°). The 2-detector system yields more counts from ~0°–70° and 140°–180°, while the 3 detector systems lead to higher counts between ~ 70°–140°. Additionally, the total counts for the 4, 5 and 6 detector systems are lower than the 2 and 3 detector systems. Clearly, the detector surface areas and the occlusion from the other detectors have a significant impact on the detector response.

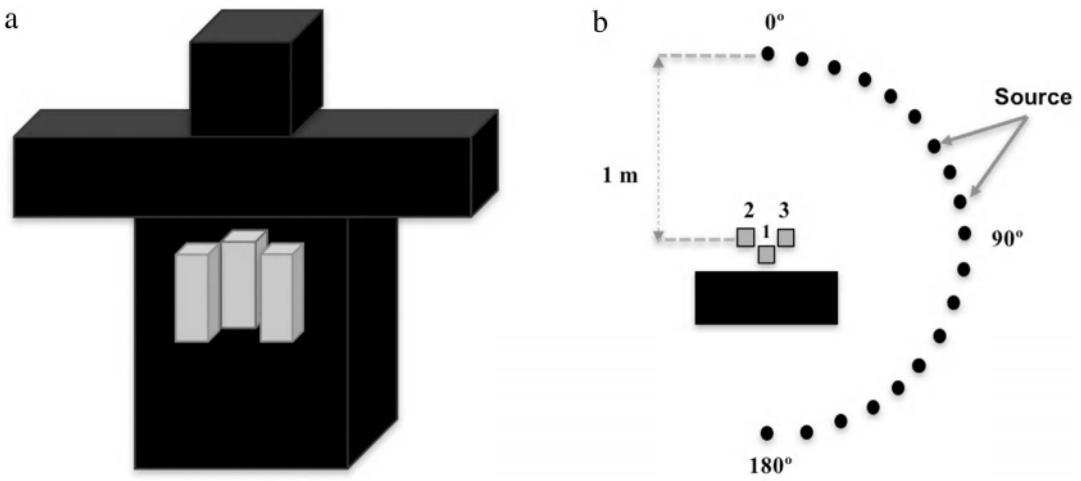


**Fig. 1.** (a) Perspective view of the simulated body phantom and detector geometry comprised of 3 RPP detector crystals. (b) Top view of the model showing the placement of a Cs-137 source (also referred to as 662 keV source) between 0° and 180° at 10° increments.

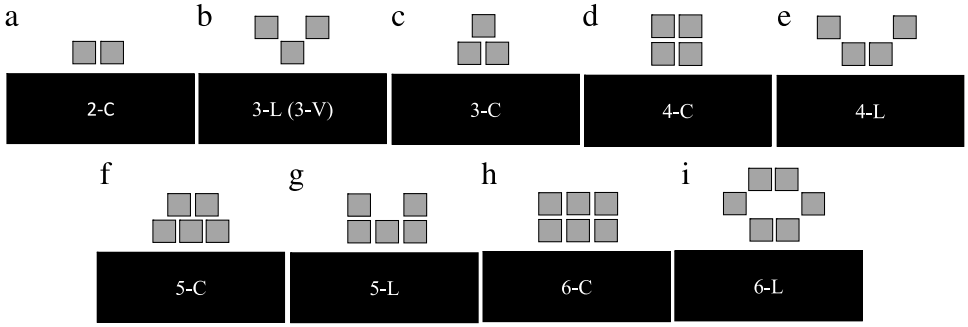


**Fig. 2.** Top view of the simulated configurations for (a) 2 detectors in a compact configuration (2-C); (b) 3 detectors in a loose, V shape (referred to as 3-L); (c) 3 detectors in a compact configuration (3-C); (d) 4 detectors in a compact configuration (4-C); (e) 4 detectors in a loose configuration, (f) 5 detectors in a compact configuration, (g) 5 detectors in a loose configuration (5-L); (h) 6 detectors in a compact configuration (6-C); and (i) 6 detectors in a loose configuration (6-L).

**Table 1**
The selected gamma-ray detector dimensions for two selected detector materials and two selected masses in particular configurations.

| Detector material | Number of detectors | Source Energy (keV) | Detector shape | Detector cross sectional area for RPP/RCC ($cm^2$) | Detector height (cm) | |
|---|---|---|---|---|---|---|
| | | | | | 3 kg RPP/RCC | 4 kg RPP/RCC |
| CLYC | 2 | 662 | RPP/RCC | $5.08\times5.08/2.54^2\ \pi$ | 17.56/22.37 | 23.41/29.83 |
| CLYC | 3 | 662 | RPP/RCC | $5.08\times5.08/2.54^2\ \pi$ | 11.71/14.91 | 15.61/19.88 |
| CLYC | 3 | 662 | RCC | $3.81^2\ \pi$ | NA* | 8.84 |
| CLYC | 3 | 122, 662, 1332 | RPP | $5.38\times5.38$ | 10.44/NA | 13.92/NA |
| CLYC | 4 | 662 | RPP/RCC | $5.08\times5.08/2.54^2\ \pi$ | 8.78/11.19 | 11.71/14.91 |
| CLYC | 5 | 662 | RPP | $5.08\times5.08$ | NA | 9.37 |
| CLYC | 6 | 662 | RPP | $5.08\times5.08$ | NA | 7.80 |
| CsI | 2 | 662 | RPP/RCC | $5.08\times5.08/2.54^2\ \pi$ | 12.89/16.42 | 17.18/21.89 |
| CsI | 3 | 122, 662, 1332 | RPP/RCC | $5.08\times5.08/2.54^2\ \pi$ | 8.59/10.95 | 11.46/14.59 |
| CsI | 3 | 662 | RPP/RCC | $4.5\times4.5/2.54^2\ \pi$ | 10.95/13.95 | 14.60/18.60 |
| CsI | 3 | 662 | RPP | $4.0\times4.0/2.0^2\ \pi$ | 13.86/NA | 18.48/NA |
| CsI | 4 | 662 | RPP/RCC | $5.08\times5.08/2.54^2\ \pi$ | 6.44/8.21 | 8.59/10.95 |

* Not analyzed.

The "peak-to-total ratio" is another desirable parameter in a detection system used for radioisotope identification. Fig. 4(b) shows the angular distribution of the average (over the number of detectors in the system) peak-to-total ratio. From the figure, one can draw a conclusion that overall the 3-L detector system has the best peak-to-total ratio compared to the other candidate designs. The ratios are lower when the source is behind the phantom (150°–180°).

### 2.2. Directionality inference and uncertainty quantification

A *k*-Nearest Neighbors (*k*NN) algorithm [20] was used to estimate the directional uncertainty for proposed detector array geometries. *k*NN is a supervised learning approach which gives the *k* most similar training samples votes to classify a test sample. In *k*NN, training samples themselves are used to define what constitutes a class. During classification, *k*NN will compare the sample in question against the classes it has defined by measuring the Euclidean distance (quantifying how different the sample is) from all the training samples. The testing sample is finally classified by tallying the votes of the *k* least different training samples compared to the test sample. In this analysis, the *k* parameter is set to one, or in other words, the testing sample will be classified to the training sample to which it is most similar.

The simulations described in Section 2.1 comprise the training data sets for each configuration. Synthetic radiation sensing data for

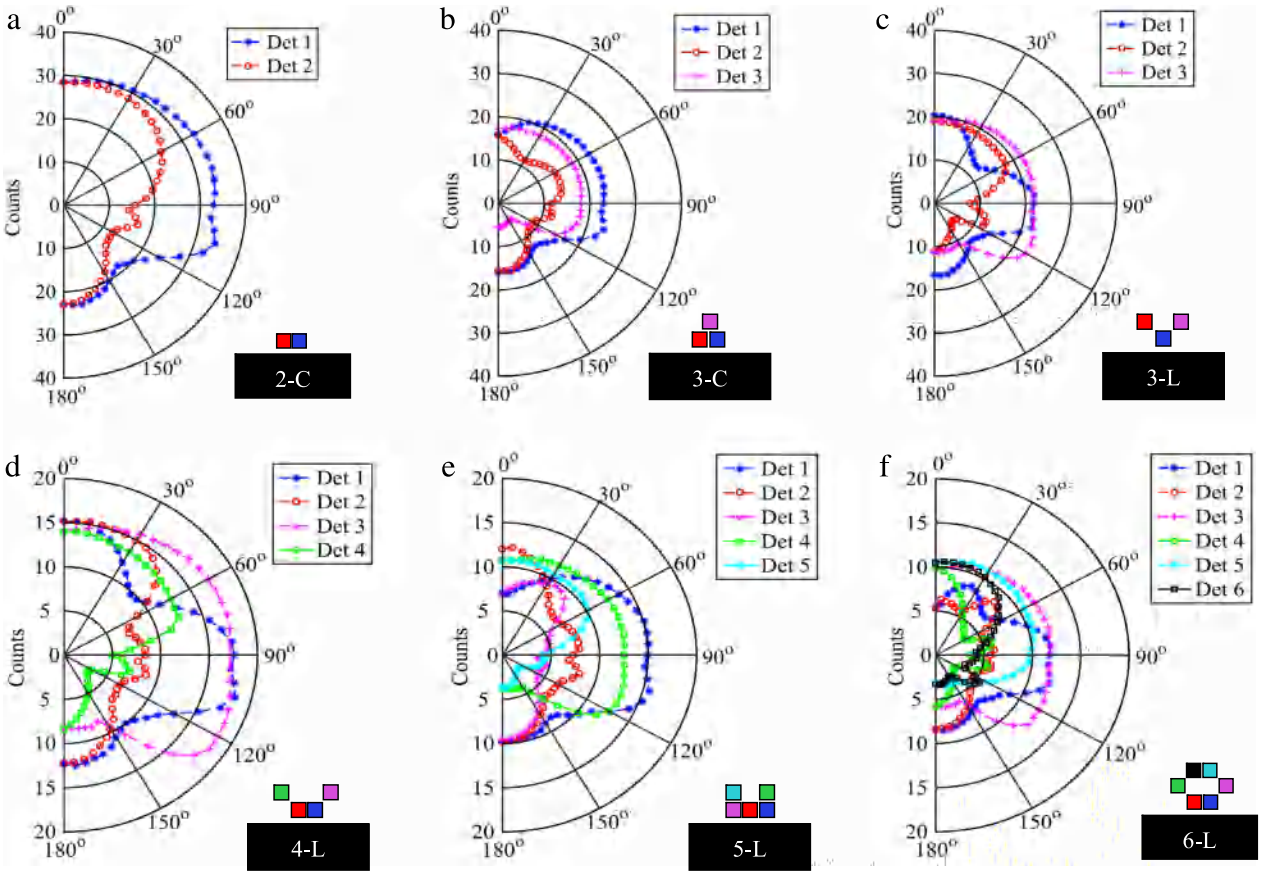


**Fig. 3.** Angular detector responses for (a) 2-C, (b) 3-C, (c) 3-L, (d) 4-L, (e) 5-L, and (f) 6-L configurations in a 4 kg CLYC detector array. Note that the scales are consistent for (a)–(c) and (d)–(f), respectively.

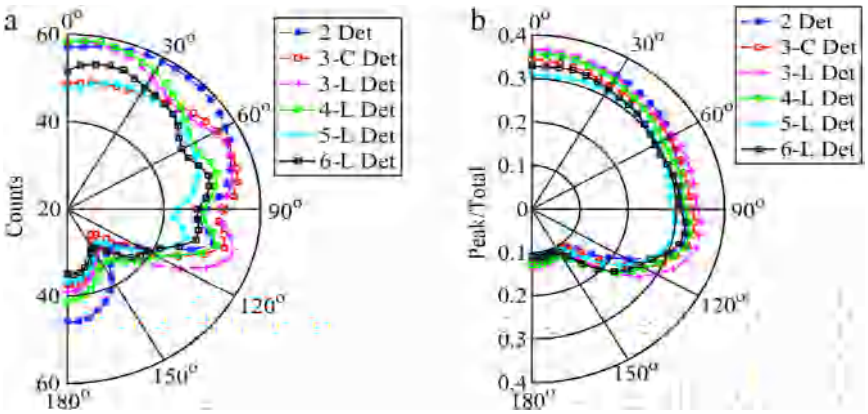


**Fig. 4.** Distribution of (a) total counts and (b) peak-to-total ratios for the 2-C, 3-C, 3-L, 4-L, 5-L and 6-L configuration of 4 kg CLYC detector arrays. The source strength is 1 $\mu$Ci of $^{137}$Cs.

**Table 2**
Feature for directionality classification.

| Number of detectors | Number of features | Feature definitions $\left(\frac{\det index}{\det index}\right)$ |
|---|---|---|
| 2 | 1 | $\frac{2}{1}$ |
| 3 | 3 | $\frac{2}{1}, \frac{3}{1}, \frac{3}{2}$ |
| 4 | 6 | $\frac{2}{1}, \frac{3}{1}, \frac{4}{1}, \frac{3}{2}, \frac{4}{2}, \frac{4}{3}$ |
| 5 | 10 | $\frac{2}{1}, \frac{3}{1}, \frac{4}{1}, \frac{5}{1}, \frac{3}{2}, \frac{4}{2}, \frac{5}{2}, \frac{4}{3}, \frac{5}{3}, \frac{5}{4}$ |
| 6 | 15 | $\frac{2}{1}, \frac{3}{1}, \frac{4}{1}, \frac{5}{1}, \frac{6}{1}, \frac{3}{2}, \frac{4}{2}, \frac{5}{2}, \frac{6}{2}, \frac{4}{3}, \frac{5}{3}, \frac{6}{3}, \frac{5}{4}, \frac{6}{4}, \frac{6}{5}$ |

the testing sample was generated by selecting a random source angle between 0 and $\pi$ and interpolating the simulated results for a 1 s acquisition to the appropriate value. A source strength was then chosen randomly between 0 and 200 $\mu$Ci and used as a scale factor for the simulated 1-$\mu$Ci detector responses. The resulting expected total count value for each detector was then subjected to Poisson sampling in order to account for statistical noise. The resulting detector counts were then converted into count ratios by dividing the counts from one detector

by another in a combinatorial fashion, as detailed in Table 2. More details on the synthetic data generation procedure, the rationale behind converting the synthetic counts into the features, the computational burden of finding the uncertainty's lower limit, and other details in using this data driven approach can be found in [12].

The uncertainty metric used to score an entire detector array is the weighted Bayes Error Rate. Given $n$ samples, the probability of an observed measurement, $T$, under the assumption that it belongs to class $\theta$, is defined as $p(T|\theta)$, which is defined using a training set with ground truth information. In this analysis, we consider each class's probability density function (pdf), $p(T|\theta)$, to be normally distributed and use synthetic data to define each pdf (see Ref. [12] for more detail). This probability is weighted by the physical distance away from ground truth, $(|\hat{\theta}(T) - \theta|)$, which yields the average uncertainty, $u_\theta = \sum_{i=0}^{n} p(T|\theta)\,|\hat{\theta}(T) - \theta|$. This weighted error is summed across all the samples to generate the uncertainty values in the Directionality Bayesian Uncertainty column found in Tables 3 and 4. Note that in this application it is important to keep track of physical distance. For instance, the distance between 350° and 10° is 20°. The results of these efforts yield the average directionality uncertainty metric, $u_\theta = \Sigma_{i=1}^{n} p(T|\theta)\,|\hat{\theta}(T) - \theta|$, which is used in the discussion of Section 2.4.

### 2.3. Gain stabilization study

Any fieldable gamma sensitive spectroscopy system which relies on photopeak information requires a mechanism to account for gain drift during operation. This is important for isotope identification, as well as any detection or localization methods that rely on photopeak counts. One common gain stabilization method takes advantage of the 1461-keV peak from K-40 that is naturally present in the background. Due to the statistical error inherent to radiation counting, each detector element must be efficient enough at 1461 keV in order to maintain gain stabilization with some desired accuracy. This work does not account for any systematic effects inherent to a particular hardware implementation.

In our work, we investigated the expected ability to estimate the photopeak centroid from data collected every two minutes, given statistical uncertainty. MCNP6.1 simulations of all detector configurations were conducted. Our MCNP6.1 simulations used a 6 m × 6 m × 1m (depth) soil ($\rho_{soil} = 1.82$ g/cm$^3$) slab to generate gamma-ray background radiation for the detector array configurations listed in Table 1. These dimensions were chosen to maximize computation efficiency; larger soil volumes would require significantly more computational time while the result would not change significantly. The main constituents of the soil were Oxygen, Silicon, Aluminum, Iron, Calcium, Sodium, Magnesium and Potassium. $^{40}$K, $^{235+232}$U and $^{232}$Th were included in the soil source model used since they may contribute to the 1461 keV peak via downscattering. The soil slab was located 1 m below the backpack center, and the soil activity was taken to be 238.7 gammas per second emitted per kilogram of soil. A Gaussian fit was applied to the simulated spectra such that the centroid could be determined for many two-minute counting intervals. The distribution of centroids represents the expected stability of the detection system. While no sources of gain instability are included in these simulations, by calculating the photopeak centroid distribution, we can assess the ability to properly identify the $^{40}$K peak in the limit of low statistics. In this work, we used the root mean squared error (RMSE) of the calculated 1461 keV centroid in units of gain percent as the metric for gain stabilization. The potassium peak can be consistently identified in two-minute collection intervals within the spectra.

### 2.4. Constrained optimization and tradeoff discussion for gamma-ray sensing

In our work, we set our design selection priority in the following order: (1) sensitivity via total counting, (2) directionality, (3) peak-to-total ratio, (4) gain stability, and (5) system simplicity. Priorities need to be set in order to made selections among the various tradeoffs.

Tables 3 and 4 show the results for the CLYC and CsI:Na detector configurations, respectively. The total counts and the peak-to-total ratio values were normalized to the highest value for 4 kg of CLYC, while the normalization for CsI:Na is for 3 kg. The CsI:Na data was normalized to 3 kg because the neutron detector will add extra mass, so for 4 kg of total detector mass, an optimized gamma-ray detector should be closer to 3 kg. Clearly, 4 kg of detectors perform better than 3 kg of detectors where any individual detector is less than 3 or 4 kg.

Referring to Table 3, one can see that increasing the number of detectors tends to improve expected localization performance while decreasing sensitivity, peak-to-total ratio, and gain stability. For example, the expected error in directionality estimation for the 6-L RPP case is very low at 3.43°, while the normalized total counts and normalized peak-to-total ratio are both relatively low (0.86 and 0.81, respectively) and the expected gain shift is relatively high at 0.27%. On the other hand, the expected performance of the two-RPP detector system includes high sensitivity with an expected total count of 0.94, a high normalized peak-to-total ratio of 0.88, and a low gain shift (0.15%), but poor directionality uncertainty of 45.61° is expected.

Increasing from two to three detectors yields the best of most desired performance characteristics. In particular, the 3-L RPP configuration with a 5.38×5.38 cm$^2$ cross section is expected to yield very high total counts (0.94), high peak-to-total ratio (0.93 normalized), relatively low directional uncertainty (8.11°) and a low gain shift (0.17%). When this configuration was compared to 3-L RCC configuration with a 3.81$^2$ $\pi$ cm$^2$ cross section, one can see that it has the highest peak-to-total ratio (1.00 normalized) but relatively low total counts (0.83) and directionality uncertainty of (8.84°).

As one would expect, when the source energy is decreased to 122 keV, the normalized total counts (1.31) and peak-to-total ratio (2.03) are expected to outperform the 662 keV case. Referring to Table 3, this is shown for the 3-L RPP configuration. However, the expected directionality uncertainty of (28.44°) for this case showed that the performance is much worse than in the 662 case (8.11°) when the training data is at 662 keV. At higher energies (1332 keV) the performance at total counts (0.77) and peak-to-total ratio (0.59) are worse, but performance is better at the directionality error estimation (17.66°) when compared to the 122 keV case. On the other hand, when the models were trained for 122 keV and tested for 122 keV the directionality uncertainty decreased significantly to only 4.36°. When data were trained with 1332 keV and tested for 1332 keV the error in directionality estimation decreased to 11.36°.

These results reveal the dependence of directionality performance on the assumption of incident radiation. If the incoming photon generates the measured counts differently to how the photon is assumed to generate the counts, a systematic bias is introduced to directionality. This systematic bias arises from the incorrect leverage of information to classify the incident photon. Fig. 5 shows the simulated detector array results for a 200 $\mu$Ci source which emits either a 662-keV, 122-keV or 1332-keV photon. A 122-keV photon generates detector responses different to a 662-keV photon due to the difference of the nature of interaction. At 122 keV, the counts are primarily generated by photoelectric absorptions and incoherent scatters. Photoelectric absorptions guarantee a single count per incident photon, while incoherent scatters involve very few counts per incident photon. A 662-keV photon's count contributions arise primarily from incoherent scattering, there are more counts generated per incident photon, as the photon generally scatters down to lower energies before it is absorbed. In the context of classifying 122-keV photons while expecting 662-keV photons, the $k$NN algorithm is expecting smoother detector response profiles, such as Fig. 5(a), with multiple counts per incident photon and increased scattering between the detectors. However, in this scenario fewer counts are experienced due to the absorptions, leading to a different detector response profile shown in Fig. 5(b), where sharp decreases in counts are seen where a detector blocks another's view of the source producing sharper count rate curves in comparison to Fig. 5(a).

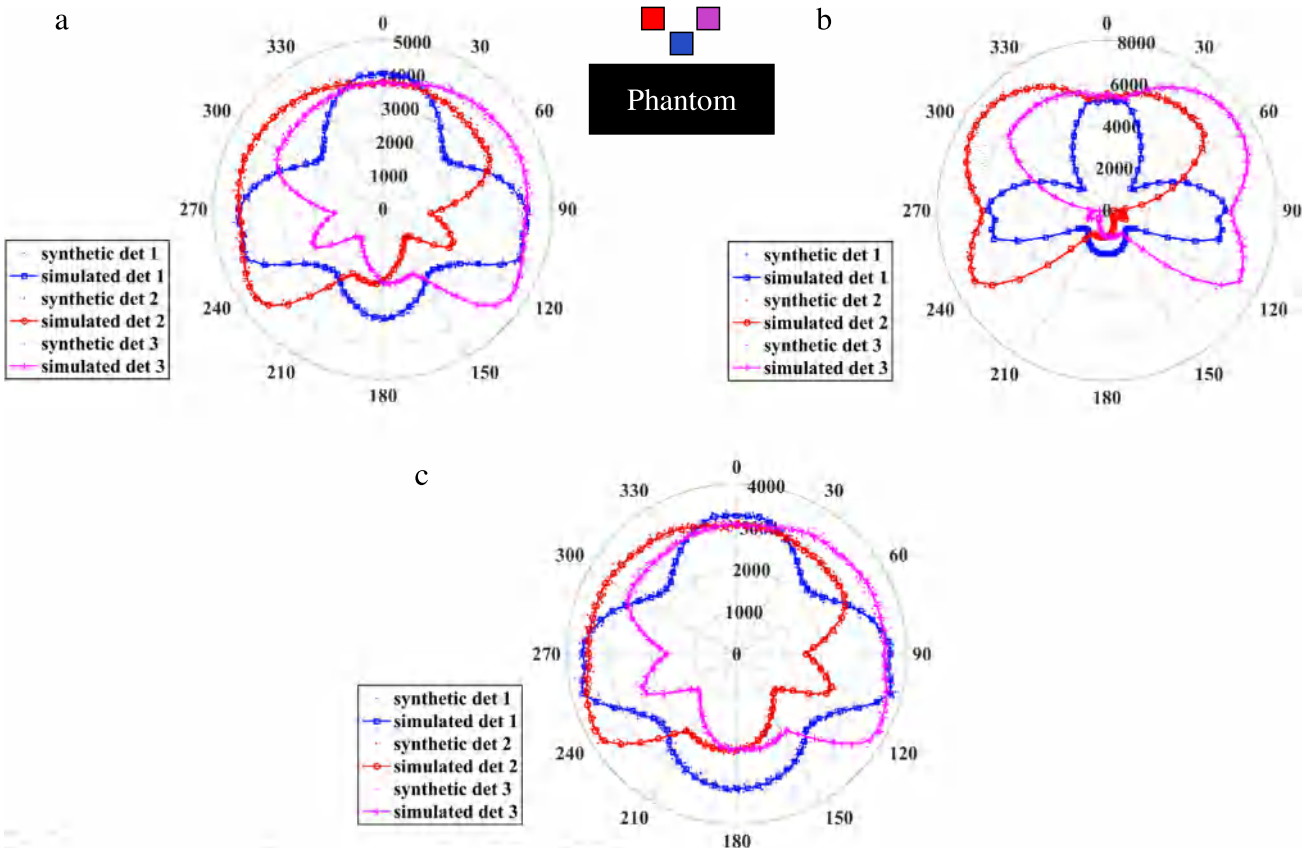


**Fig. 5.** Simulated detector array results for a 200-$\mu$Ci source. (a) Array response due to 662-keV incident photons (b) Array response due to 122-keV incident photons, (c) The array response due to 1332-keV incident photons at 1 m.

**Table 3**
Simulated CLYC detector data for constrained optimization and tradeoff study.

| Number of detectors/configuration | Detector shape | Detector cross section ($cm^2$) | Source energy | Bayesian directionality mean error (%) | | Gain stabilization (gain %) RMSE | | Normalized total counts @ 0 ° | | Normalized peak-to-total @ 0 ° | |
|---|---|---|---|---|---|---|---|---|---|---|---|
| | | | | 3 kg | 4 kg | 3 kg | 4 kg | 3 kg | 4 kg | 3 kg | 4 kg |
| 2 | RPP | 5.08×5.08 | 662 | 46.63 | 45.61 | 0.18 | 0.15 | 0.72 | 0.94 | 0.86 | 0.88 |
| 2 | RCC | $2.54^2\ \pi$ | 662 | 49.22 | 46.63 | 0.18 | 0.18 | 0.76 | 1.00 | 0.83 | 0.85 |
| 3-L | RPP | 5.08×5.08 | 662 | 9.79 | 8.94 | 0.22 | 0.18 | 0.73 | 0.97 | 0.88 | 0.91 |
| 3-L | RCC | $2.54^2\ \pi$ | 662 | 10.75 | 9.07 | 0.24 | 0.20 | 0.75 | 0.99 | 0.83 | 0.86 |
| 3-C | RPP | 5.08×5.08 | 662 | 15.28 | 13.80 | 0.24 | 0.19 | 0.62 | 0.81 | 0.82 | 0.85 |
| 3-C | RCC | $2.54^2\ \pi$ | 662 | 18.07 | 16.36 | 0.23 | 0.20 | 0.68 | 0.90 | 0.81 | 0.83 |
| 3-L | RPP | 5.38×5.38 | 662 | NA | 8.11 | 0.21 | 0.17 | NA | 0.94 | NA | 0.93 |
| 3-C | RPP | 5.38×5.38 | 662 | NA | 12.77 | 0.23 | 0.19 | NA | 0.78 | NA | 0.87 |
| 3-L | RCC | $3.81^2\ \pi$ | 662 | NA | 8.84 | NA | NA | NA | 0.83 | NA | 1.00 |
| 4-C | RPP | 5.08×5.08 | 662 | 6.58 | 5.65 | 0.28 | 0.24 | 0.56 | 0.74 | 0.79 | 0.77 |
| 4-C | RCC | $2.54^2\ \pi$ | 662 | 6.66 | 5.93 | 0.28 | 0.24 | 0.61 | 0.80 | 0.79 | 0.76 |
| 4-L | RPP | 5.08×5.08 | 662 | NA | 4.80 | 0.26 | 0.22 | 0.73 | 0.97 | 0.90 | 0.88 |
| 5-C | RPP | 5.08×5.08 | 662 | NA | 4.60 | 0.32 | 0.27 | NA | 0.79 | NA | 0.77 |
| 5-L | RPP | 5.08×5.08 | 662 | NA | 4.51 | 0.31 | 0.26 | NA | 0.79 | NA | 0.76 |
| 6-C | RPP | 5.08×5.08 | 662 | NA | 5.28 | 0.35 | 0.30 | NA | 0.75 | NA | 0.72 |
| 6-L | RPP | 5.08×5.08 | 662 | NA | 3.43 | 0.34 | 0.27 | NA | 0.86 | NA | 0.81 |
| 3-L | RPP | 5.38×5.38 | 122[a] | NA | 28.44 | NA | NA | NA | 1.31 | NA | 2.03 |
| 3-L | RPP | 5.38×5.38 | 122[b] | NA | 4.96 | NA | NA | NA | 1.31 | NA | 2.03 |
| 3-L | RPP | 5.38×5.38 | 1332[a] | NA | 17.66 | NA | NA | NA | 0.77 | NA | 0.59 |
| 3-L | RPP | 5.38×5.38 | 1332[c] | NA | 11.26 | NA | NA | NA | 0.77 | NA | 0.59 |

[a] Data trained at 662 keV.
[b] Data trained at 122 keV.
[c] Data trained at 1332 keV.

For the case of a 1332-keV photon while expecting a 662-keV photon, the directionality performance decreases less than the 122-keV case since the counts are generated in a similar fashion to the 662-keV case. The attenuation coefficients are similar between the 662-keV and 1332-keV cases; however, the counts are generated through both incoherent scattering and pair production at the higher energy. These factors contribute to less sensitivity to occlusion which manifests as smoother curves as shown in Fig. 5(c).

The data for CsI:Na in Table 4 shows similar trends compared with the CLYC data shown in Table 3. For a fixed total crystal mass of 3 kg,

the 3-L RPP configuration with a 5.08×5.08 $cm^2$ cross section produces expected normalized total counts of 0.89, the highest peak-to-total ratio (1.00 normalized), relatively low error in directionality estimation (9.53%), and low gain shift (0.29%). The other good candidate out of those considered is 3-L RCC detectors with a $2.54^2\pi$ cross section. This system has high expected total counts (0.91) and peak-to-total ratio (0.98 normalized), as well as low expected directionality estimation error (9.58%) and gain shift (0.30%). The 122-keV and 1332-keV studies with 3-L detectors, 5.08×5.08 $cm^2$ or $2.54^2\pi$ $cm^2$ showed similar behavior compared to what was observed with the CLYC cases. In the 3-L RCC configuration, the directionality estimation errors at 122 keV and 1332 keV are expected to be higher than the 662 keV case when the data is trained at 662 keV.

Generally speaking, CLYC outperforms CsI:Na on gain stabilization and total counts while CsI:Na outperforms CLYC on peak-to-total ratio when their masses are the same. The behavior in directionality estimation is slightly in favor of CsI:Na for the 3- and 4-detector cases while CLYC has better response in the two-detector case. For example, when we examine 4-kg 3-L RPP 5.08×5.08 $cm^2$ detectors, the errors for directionality estimation for CLYC and CsI:Na are 8.94% and 8.01% respectively. On the other hand, the gain shift for CLYC and CsI:Na are 0.18% and 0.25%.

The total counts and peak-to-total ratio normalization between CLYC and CsI:Na showed that total count in CLYC configurations surpass CsI:Na between 20%-49% depending on the detector configuration (identical configurations were compared with each other). On the other hand, CsI:Na surpasses CLYC in peak-to-total ratio, as expected given its higher density. CsI:Na detectors systems were between 18%–25% better than CLYC detection systems.

Also, if the RPP detectors performance is compared to the RCC detectors one can see that in general RPP detectors perform better in peak-to-total ratio and directionality estimation while RCC detectors performs better in total counts. The performance in gain stabilization does not have a clear winner. For example, the 4-kg CLYC 2 RPP detectors have directionality estimation error of 45.61%, normalized total counts of 0.94 and peak-to-total ratio as 0.88 respectively. On the other hand, the 4-kg CLYC 2 RCC detectors have directionality estimation error of 46.63%, normalized total counts of 1.00 and peak-to-total ratio of 0.85, respectively. The other examples are the 3-kg CsI:Na with 3-L RPP and 3-L RCC detectors. 3-L RPP detectors are expected to have slightly better directionality estimation (9.53% vs. 9.58%), lower normalized total counts (0.89 vs 0.91) and a higher peak-to-total ratio (1.00 vs 0.98).

### 2.5. Monte Carlo simulations for neutron sensing

The neutron detector necessarily takes up some of the available mass of a wearable system for radiological and nuclear threat sensing and must simply function as a $^3$He replacement in this system, able to count neutrons with high efficiency and excellent gamma rejection, such that gammas are not mistaken as neutrons. It is not a goal of this design for the neutron detector to provide directionality. There may not be a good solution for a subsystem of such low mass to provide directionality for relevant neutron sources in time periods $O$ (1 s). It is a goal, however, to present practical, wearable $^3$He alternatives for the directionally-capable gamma detector arrays that are studied here.

The selected CLYC-based gamma-ray detection system (3-L RPP with 5.38×5.38 $cm^2$ cross section) could be also used as a neutron detector if enriched $^6$Li is used. On the other hand, the CsI array requires the addition of a neutron detector subsystem in order to operate as a hybrid detector array with sensitivity to a broad array of radiological and nuclear threats. In particular, we posit that TRUST-type LiCAF [17,18] would be a good choice in a lightweight, wearable system since it is flexible and can be produced in large sizes with 95% enriched $^6$Li.

MCNP6.1 simulations were used (1) to understand the expected neutron detection performance of the selected CLYC design and (2) to design a LiCAF rubber neutron detector subsystem to be used with a directional CsI gamma-ray detection array. Various sizes of LiCAF rubber detectors with different weight ratios of rubber and LiCAF were simulated. The goal was to maximize the total neutron capture while retaining the flexibility. This simulation-based study does not address gamma-ray rejection performance, but let the reader note that our design selections are expected to be acceptable $^3$He alternatives, as described in [21].

The MCNP6.1 geometry for this study starts with the same phantom used in our gamma-ray optimization studies. A $^{252}$Cf source surrounded with 3 cm of stainless steel, 0.5 cm of lead, and 4 cm of High Density Poly Ethyl (HDPE) was located 1.5 m away from the detector center, as described in ANSI_42.53-2013 [19]. Since the neutron detection subsystem is not expected to yield any source directional information over acquisition intervals of order 1 s, the simulations were performed only for 0° (see Fig. 1(b)). The expected neutron detection efficiency was tallied from the total number of capture reactions by using a F8 tally with the FT8 CAP option. The detectors were located 3 cm away from the phantom (body).

In order to estimate $^3$He detection equivalence, another MCNP6.1 simulation set was performed to calculate the volume of $^3$He that yields the expected neutron detection efficiency obtained from either the selected CLYC detection system or a TRUST-type LiCAF detector subsystem. The LiCAF subsystem was assumed to be right next to the back of the wearer (or phantom). To study detection equivalence, we modeled 6–9 $^3$He detectors placed side-by-side for this comparison, each pressurized to 3 atm and lined up with the back of the phantom.

Fig. 6 compares the expected performance for the selected CLYC detector system, various sizes of flexible LiCAF detectors, and $^3$He detectors. The neutron capture response from 3-L RPP CLYC detectors, a 360 $cm^2$ area of 65% LiCAF + 35% rubber (20×18×0.5 $cm^3$), or one of two configurations of 600 $cm^2$ of LiCAF rubber are compared to 1.95 L of $^3$He, 3.08 L of $^3$He, or 3.49 L of $^3$He. The two larger area LiCAF configurations – although not too large for a backpack – include 65% LiCAF +35% rubber (30×20×0.5 $cm^3$) and 32.5% LiCAF + 67.5% rubber (30×20×1 $cm^3$). While the 360 $cm^2$ area of LiCAF is expected to be approximately efficient to the 3 CLYC detectors or to 1.95 L of $^3$He, we chose an area of 600 $cm^2$ (30×20 $cm^2$) in our proposed design in order to maximize the neutron detector surface area, and this size is reasonable for a backpack. The 32.5% LiCAF, 1 cm thick detector, although its mass is greater, may have better gamma-ray rejection than 65% LiCAF [22], so we simulated both designs. The 1 cm thick design is expected to be equivalent to 3.08 L of $^3$He, while the 0.5 cm thick design is equivalent to 3.49 L of $^3$He. A hybrid wearable system could be comprised, for example, out of ~3 kg of CsI in the 3-L RCC configuration + 0.744 kg of LiCAF neutron detector comprised of 32.5% LiCAF + 67.5% rubber (30×20×1 $cm^3$, 600 $cm^2$). While its neutron detection would likely be better than the selected CLYC configuration (3-L RPP with 5.38×5.38 $cm^2$ cross section), its gamma-ray sensing performance is expected to be somewhat degraded.

## 3. Conclusions

For any wearable system capable of detecting, localizing, and identifying a broad array of radiological and nuclear threat sources, there are competing design priorities at play. Our simulation-based constrained optimization and tradeoff study showed that a wearable radiation array, consisting of 4 kg of three right-parallelepiped-shaped CLYC detectors, each of dimension 5.38×5.38×13.92 $cm^3$, arranged in a loose V-configuration, is expected to perform well (see Table 3) in terms of expected total gamma-ray and neutron counting efficiencies, directionality estimation, peak-to-total ratio, and gain stability (based on detection of 1461 keV K-40 gammas). We suppose that good directionality capability (say, if source and detector system are stationary) should lead to good source localization performance (even if source and or detector system are moving).

**Table 4**
Simulated CsI:Na detector data for constrained optimization and tradeoff study.

| Number of detectors/configuration | Detector shape | Detector cross section ($cm^2$) | Source energy | Bayesian directionality Bayesian error rate (%) | | Gain stabilization (gain %) RMSE | | Normalized total counts @ 0 ° | | Normalized peak-to-total @ 0 ° | |
|---|---|---|---|---|---|---|---|---|---|---|---|
| | | | | 3 kg | 4 kg | 3 kg | 4 kg | 3 kg | 4 kg | 3 kg | 4 kg |
| 2 | RPP | 5.08×5.08 | 662 | 49.66 | 48.92 | 0.26 | 0.22 | 0.86 | 1.13 | 0.99 | 1.02 |
| 2 | RCC | $2.54^2\ \pi$ | 662 | 51.41 | 50.25 | 0.25 | 0.22 | 0.93 | 1.22 | 0.98 | 1.00 |
| 3-L | RPP | 5.08×5.08 | 662 | 9.53 | 8.01 | 0.29 | 0.25 | 0.89 | 1.17 | 1.00 | 1.04 |
| 3-L | RCC | $2.54^2\ \pi$ | 662 | 9.58 | 8.60 | 0.30 | 0.27 | 0.91 | 1.19 | 0.98 | 1.00 |
| 3-L | RPP | 4.5×4.5 | 662 | 10.07 | 8.76 | 0.30 | 0.27 | 0.94 | 1.24 | 0.97 | 1.00 |
| 3-L | RCC | $2.25^2\ \pi$ | 662 | 10.64 | 9.44 | 0.31 | 0.28 | 0.98 | 1.29 | 0.95 | 0.97 |
| 3-L | RPP | 2.0×2.0 | 662 | 10.58 | 9.17 | 0.31 | 0.27 | 1.00 | 1.32 | 0.94 | 0.96 |
| 3-C | RPP | 5.08×5.08 | 662 | 14.34 | 12.38 | 0.31 | 0.26 | 0.72 | 0.94 | 0.93 | 0.97 |
| 3-C | RCC | $2.54^2\ \pi$ | 662 | 17.34 | 15.81 | 0.32 | 0.26 | 0.81 | 1.06 | 0.94 | 0.97 |
| 3-C | RPP | 4.5×4.5 | 662 | 17.14 | 15.29 | 0.32 | 0.28 | 0.75 | 0.99 | 0.90 | 0.93 |
| 4-C | RPP | 5.08×5.08 | 662 | 6.60 | 5.81 | 0.36 | 0.31 | 0.63 | 0.82 | 0.83 | 0.88 |
| 4 -C | RCC | $2.54^2\ \pi$ | 662 | 6.59 | 5.66 | 0.35 | 0.31 | 0.70 | 0.92 | 0.85 | 0.88 |
| 4-L | RPP | 5.08×5.08 | 662 | 6.21 | NA | 0.34 | NA | 0.90 | NA | 0.96 | NA |
| 3-L | RPP | 5.08×5.08 | 122[a] | 26.38 | NA | NA | NA | 1.16 | NA | 1.57 | NA |
| 3-L | RPP | 5.08×5.08 | 122[b] | 6.50 | NA | NA | NA | 1.16 | NA | 1.57 | NA |
| 3-L | RPP | 5.08×5.08 | 1332[a] | 17.78 | NA | NA | NA | 0.73 | NA | 0.67 | NA |
| 3-L | RPP | 5.08×5.08 | 1332[c] | 12.64 | NA | NA | NA | 0.73 | NA | 0.67 | NA |
| 3-L | RCC | $2.54^2\ \pi$ | 122[a] | 28.32 | NA | NA | NA | 1.16 | NA | 1.61 | NA |
| 3-L | RCC | $2.54^2\ \pi$ | 1332[a] | 23.63 | NA | NA | NA | 0.75 | NA | 0.64 | NA |

[a] Data trained at 662 keV.

[b] Data trained at 122 keV.

[c] Data trained at 1332 keV.

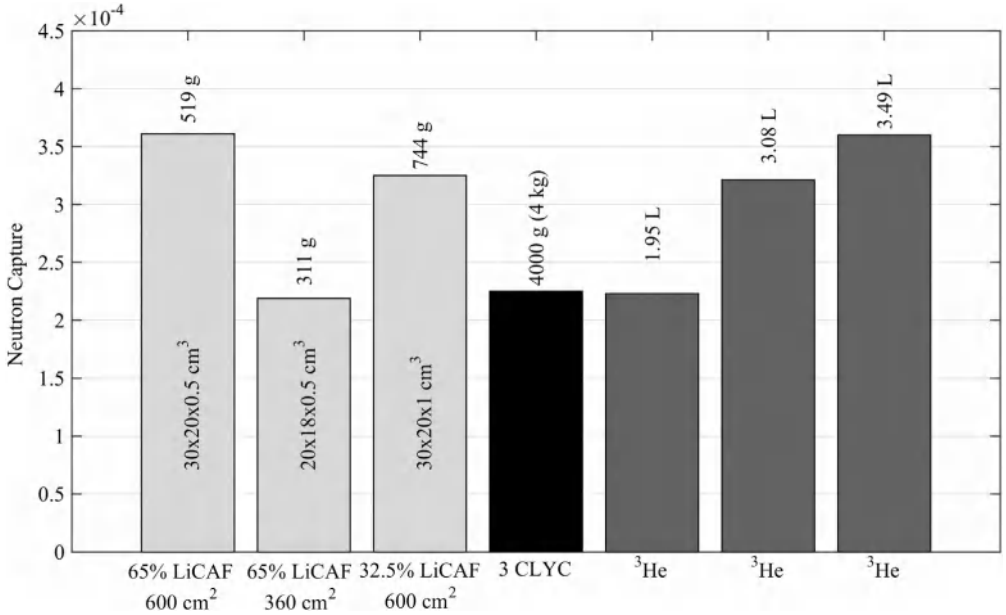


**Fig. 6.** Performance of the neutron capture events for the selected CLYC detector system, various sizes of TRUST-type LiCAF detectors, and $^3$He detectors.

Our second proposed feasibility design consists of either 3 kg of right parallelepiped-shaped CsI detectors, each of dimension 5.08×5.08×8.59 $cm^3$, or 3 kg of right circular cylinder-shaped CsI detectors, each of dimension $2.54^2\ \pi$ × 10.95 $cm^3$, arranged in a V-configuration (see results in Table 4). Along with these CsI gamma-ray detectors, one could use a TRUST-type LiCAF detector with 30×20×1 $cm^3$ dimension (0.744 kg) and 32.5% scintillator loading as a $^3$He replacement for neutron source search. Our simulation results showed that this feasibility design is expected to have the equivalent neutron capture response of 3.08 L of $^3$He (see Fig. 6).

In general, RPP-shaped detectors are expected to perform better in peak-to-total ratio and directionality estimation while RCC-shaped detectors are expected to perform better in terms of total efficiency. Comparing our two different feasibility designs, our selected CLYC-based design is expected to outperform our CsI-based designs of equal mass in the areas of gain stabilization and total efficiency, while our CsI-based designs are expected to outperform our CLYC design in peak-to-total ratio.

The two proposed feasibility designs are relatively simple, especially compared to more complex imaging instruments that are based upon coded aperture or scatter-based imaging, and they are expected to be buildable, albeit expensive at present, probably due to the ongoing development of the neutron-sensitive detector materials.

This study did not consider the effect of background radiation, directionality calibration based upon gamma-ray energy, directionality estimation based upon fast neutron counting (that relies of organic

scintillators), the gamma-ray rejection capability of various TRUST-type LiCAF configurations, or the temperature sensitivity of the aforementioned neutron-sensitive scintillators. Some of these topics will be investigated in our future work.

## Acknowledgment

This work has been supported by the US Department of Homeland Security, Domestic Nuclear Detection Office under competitively awarded contract DHS 2015-DN-077-ARI098.

## References

[1] K.P. Ziock, E.C. Bradley, A.M. Cheriyadat, M. Cunningham, L. Fabris, C.L. Fitzgerald, J.S. Goddard, D.E. Hornback, R.A. Kerekes, T.P. Karnowski, W.T. Marchant, R.J. Newby, IEEE Trans. Nucl. Sci. 60 (2013) 2237.
[2] B. Ayaz-Maierhafer, J.P. Hayward, K.P. Ziock, M.A. Blackston, L. Fabris, Nucl. Instrum. Methods A 712 (2013) 120–125.
[3] B.S. Budden, L.C. Stonehill, N. Dallmann, M.J. Baginski, D.J. Best, M.B. Smith, S.A. Graham, C. Dathy, J.M. Frank, M. McClish, Nucl. Instrum. Methods A 784 (2015) 97–104 Available: http://dx.doi.org/10.1016/j.nima.2014.11.051.
[4] https://www.bruker.com/fileadmin/user_upload/8-PDF-Docs/CBRNE_Detection/Literature/Backpack-Brochure-en.pdf.
[5] http://www.symetrica.com/backpack.
[6] http://www.rapiscansystems.com/en/products/radiation_detection/rapiscan_mp100.
[7] https://www.thermofisher.com/order/catalog/product/FHT1377.
[8] J.L. Lacy, A. Athanasiades, C.S. Martin, L. Sun, G.J. Vazquez-Flores, IEEE Trans. Nucl. Sci. 60 (2013) 1111.
[9] B.S. McDonald, M.J. Myjak, M.A. Zalavadia, J.E. Smart, J.A. Willett, P.C. Landgren, Ch.R. Greulich, Nucl. Instrum. Methods A 821 (2016) 73.
[10] J.M.C. Nilsson, K. Östlund, J. Söderberg, S. Mattsson, C. Rääf, J. Env. Rad. 135 (2014) 54.
[11] R.C. Runkle, M.J. Myjak, S.D. Kiff, D.E. Sidor, S.J. Morris, J.S. Rohrer, K.D. Jarman, D.M. Pfund, L.C. Todd, R.S. Bowler, C.A. Mullen, Nucl. Instrum. Methods A 598 (2009) 815.
[12] C. Britt, A.J. August, B. Ayaz-Maierhafer, E. Green, H. Qi, C. Seifert, J. Hayward, Nucl. Instrum. J. Methods (will be submitted soon).
[13] C.J. Solomon, Jr., S.R. McKigney, E.A. Bolding, Comparing radiation detection experiments to simulation with MCNP, 2013. LA-UR-13-24756.
[14] M. Sellers, J.T. Goorley, E. Corcoran, D. Kelley, MCNP6 delayed neutron emission validation with experimental measurements, presentation 2011. LA-UR-11-05868.
[15] M.M. Bourne, C. Mussi, E.C. Miller, S.D. Clarke, S.A. Pozzi, A. Gueorguiev, Nucl. Instrum. Methods A 736 (2014) 124.
[16] R. Machrafi, N. Khan, A. Miller, Radiat. Meas. 70 (2014) 5.
[17] D. Sugimoto, K. Watanabe, K. Hirota, A. Yamazaki, A. Uritani, T. Iguchi, K. Fukuda, S. Ishidu, N. Kawaguchi, T. Yanagida, Y. Fujimoto, A. Yoshikawa, H. Hasemi, K. Kino, Y. Kiyanagi, Phys. Procedia 60 (2014) 349.
[18] K. Watanabe, T. Yamazaki, D. Sugimoto, A. Yamazaki, A. Uritani, T. Iguchi, K. Fukuda, S. Ishidu, T. Yanagida, Y. Fujimoto, Nucl. Instrum. Methods A 784 (2015) 260.
[19] American National Standard performance criteria for backpack based Radiation-Detection Systems (ANSI) used for homeland security.
[20] N.S. Altman, Amer. Statist. 46 (1992) 175.
[21] R.T. Kouzes, A.T. Lintereur, E.R. Siciliano, Nucl. Instrum. Methods A 784 (2015) 172.
[22] Private communication with Takuyama Inc, Japan. https://www.tokuyama.co.jp/eng/research/.